Synthesis and catalytic application of nanorod-like FER-type zeolite

Weijiong Dai, Valérie Ruaux, Xin Deng, Wenshu Tai, Guangjun Wu, Naijia Guan, Landong Li, Valentin Valtchev

Synthesis and catalytic application of nanorod-like FER-type zeolite

Weijiong Dai[a,b], Valérie Ruaux[b], Xin Deng[a], Wenshu Tai[a], Guangjun Wu[a*], Naijia Guan[a], Landong Li[a], Valentin Valtchev[b,c*]

[a] School of Materials Science and Engineering & National Institute for Advanced Materials, Nankai University, Tianjin 300350, P. R. China; Email:wuguangjun@nankai.edu.cn

[b] Normandie Univ, ENSICAEN, UNICAEN, CNRS, Laboratoire Catalyse et Spectrochimie, 14050 Caen, France.

Email: valentin.valtchev@ensicaen.fr

[c] The ZeoMat Group, Qingdao Institute of Bioenergy and Bioprocess Technology, Chinese Academy of Sciences, Qingdao 266101, P. R. China

Nanosize dimensions have an important impact on zeolite properties and catalytic performance in particular. Herein, we develop a direct synthesis route to obtain nanosized nanorod-like ferrierite (FER) zeolite with the assistance of ammonium fluoride (NH_4F) and employing a conventional structure-directing agent (Pyrrolidine). The resultant nanorod-like FER zeolite crystals exhibit a greatly reduced diffusion path along the *c*-axis. The physicochemical properties of nanorod-like FER and its conventional micronsized plate-like counterpart were analyzed by N_2 adsorption-desorption, ^{27}Al, ^{1}H, ^{29}Si MAS NMR, NH_3-TPD, and *in situ* D_3-acetonitrile and pyridine adsorption followed by FTIR. The nanorod-like FER zeolite possesses superior characteristics in terms of larger external area, better accessibility to the acid sites, and a larger number of pore mouths per unit crystal surface than the micron-sized counterpart synthesized without NH_4F. The improved properties provide the nanorod-like FER zeolite with high selectivity and low deactivation rates in 1-butene skeletal isomerization. The thermogravimetry analysis (TGA) of the coke amounts revealed a better capability of coke tolerance of the nanorod-like FER zeolite. The *in situ* Ultraviolet–visible (UV/Vis) and Fourier transform infrared spectroscopy (FTIR) spectroscopy investigations of the organic intermediates formed on FER zeolite catalysts during the catalytic reaction further verified the enhanced catalytic activity and stability of the nanorod-like FER zeolite.

Introduction

Zeolites are microporous crystalline aluminosilicate materials.[1] They have been widely used in industry as acid catalysts due to their shape selectivity, intrinsic acidity, and high surface area.[2,3] Despite the outstanding features of zeolites, the sole presence of micropores could bring some drawbacks in practical applications, such as diffusion limitation and low accessibility to the active sites. Full use of zeolite potential requires circumventing these disadvantages, which is one of the hottest topics in zeolite chemistry lately.[4–6] An effective strategy to substantially alleviate the limitation is reducing the zeolite crystal size to nanosized range, thus reducing the pathway to and from active sites. During last two decades, many synthetic approaches have been developed to obtain nano-zeolite. Industrially relevant zeolites such as FAU,[7,8] LTL,[9] CHA,[7,10] MFI,[7,11] MOR,[7] have been successfully synthesized in nanosized form.

FER zeolite is a medium-pore zeolite with intersecting 10-membered (MR) and 8-membered ring channels. As shown in Fig.1, this kind of zeolite possesses a well-developed (100) face and very thin (001), (010) faces, showing a typical plate-like morphology. FER zeolite can be directly synthesized with various organic structure-directing agents (SDAs), such as alkylamines, cyclic amines, and alcohols.[12] As one of a few commercial zeolites, FER-type zeolite has been used in several catalytic reactions, including the skeletal isomerization,[13–15] dimethyl ether carbonylation[16,17] and catalytic cracking.[18] However, the topology and pore dimension of FER zeolite often hinder the reaction to the acid sites near the 10-MR pore mouths, and fast deactivation is often observed due to the pore blocking with organic deposits. This drawback could be minimized by reducing the diffusion path along the 10-MR channel and, therefore preparation of nanometric FER zeolite crystal is an effective alternative.

To obtain the nano-crystalline FER zeolite, several synthetic approaches have been developed. For example, Hong et al. prepared needle-like FER zeolite crystals with a diameter of ~10 nm and length of ~100 nm, by using choline and Na^+ cations as SDA.[19] Corma and co-workers successfully synthesized nanosized FER zeolite (~10-30 nm) by using the collaborative effect of two SDAs (piperidine and cetylmethylpiperidinium bromide).[20] Xiao et al. obtained ultrathin FER zeolite nanosheets (~6-8 nm) by using a small organic SDA (N,N-diethyl-cis-2,6-dimethylpiperidinium).[21] Valtchev et al. synthesized nanosized FER zeolite crystals with size of 100 nm by the addition of 3 wt% seeds in the synthesis gel.[22] The addition of surfactants such as cetyltrimethyl ammonium bromide[23] and sodium lauryl sulfate[24] was proposed to synthesize nanosized FER zeolite with crystal dimensions ~100-300 nm and ~300-500 nm, respectively. However, none of listed approaches offer a simple synthesis route using low-cost and easily available SDAs to obtain FER crystals with short diffusion path along the 10-MR channel. Hence, our motivation is to develop a direct synthesis strategy with low-cost and generally acceptable SDAs, leading to nanosized FER-type materials with a short diffusion length (<100 nm) along the 10-MR channel.

The fluorine anion is recognized as an alternative mineralizing agent to the hydroxide anion in zeolite synthesis. A particular feature of zeolite synthesis in a fluoride-containing medium is the formation of large, sometimes of millimeter size (“giant”) zeolite crystals. Recently, fluorine was proposed as a gel modifier able to control zeolite growth in a particular crystallographic direction.[25–27] The nanosized plate-like

MFI zeolite with an impressive thickness of ~10 nm along the *b*-axis was successfully obtained by using NH_4F at a specific stage of zeolite nucleation.[28] This approach is working with all members of MFI-type family: silicalite-1, Ga-MFI, and Al-MFI (ZSM-5). Thus, the as-synthesized ZSM-5 with particular morphological features exhibited substantially improved catalytic performance in methanol-to-hydrocarbons (MTH) reaction than the counterpart synthesized in hydroxyl medium.

Herein, the fluorine anion was used to control the FER zeolite synthesis, with the goal to obtain nanorod crystallites with a short diffusion path along the *c*-axis. Effects of NH_4F concentration on the synthesis of the FER zeolite and corresponding properties were investigated. Furthermore, the obtained nanorod-like FER zeolites were employed in the 1-butene skeletal isomerization reaction, an important catalytic reaction industrially used to produce fuel and rubber additives. Compared to the conventional FER zeolites, the nanorod-like FER zeolite displayed better catalytic performance in the conversion of 1-butene, selectivity to isobutene, as well as the capability of coke tolerance. The nature and dynamics of the organic deposits on the catalysts were further detected by *in situ* FTIR and UV/Vis spectroscopy, to verify the enhanced catalytic properties.

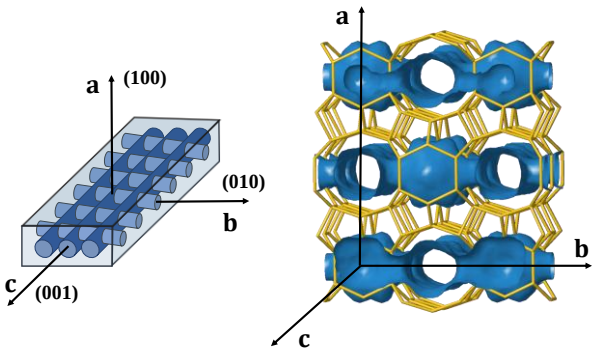

Figure 1. Left: Typical morphology of FER-type zeolite crystal with two perpendicular intersecting channels accessible via 001 (10-MR) and 010 (8-MR) faces. Right: Detail of FER-type framework with the intersections of the channels.

Experimental

Materials.

LUDOX AS-40 colloidal silica (SiO_2, 40 wt. % suspension in water, Sigma-Aldrich), Pyrrolidine (Py, 99%, Sigma-Aldrich), sodium aluminate ($NaAlO_2$, 50-56% Al_2O_3, 40-45% Na_2O, Sigma-Aldrich), Sodium hydroxide (NaOH, 99%, VWR Chemicals), NH_4F (98%, Sigma-Aldrich), NH_4Cl (99.5%, Sigma-Aldrich). The deionized water was homemade.

Synthesis.

The FER zeolite synthesis was performed from a gel with molar composition: SiO_2: $0.05Al_2O_3$: $0.08Na_2O$: 0.6Py: $20H_2O$: xNH_4F, where x is 0.1, 0.2, 0.4, 0.8, 1.2. In a typical experiment, a clearly basic solution was obtained by dissolving pyrrolidine, NaOH, and $NaAlO_2$ in deionized water. Then colloidal silica was added into the liquid and vigorously stirred at 80 ^{o}C for 12 h. Subsequently, the synthesis gel was cooled to room temperature, NH_4F was added and the mixture vigorously stirred for another 2 h. Finally, the obtained gel was transferred into an autoclave and subjected to crystallization in a tumbling oven (20 rpm) at 180 ^{o}C for 14 days. The solid products were collected by centrifugation, washed with deionized water until a near-neutral pH, and dried overnight at 60 °C. The samples synthesized with different fluoride ratio are denoted as FER-F-X, where x = 0.1, 0.2, 0.4, 0.8 and 1.2, respectively.

The FER reference sample was synthesized without a fluorine source using a gel with composition: SiO_2: $0.05Al_2O_3$: $0.08Na_2O$: 0.6Py: $20H_2O$. A clearly basic solution was firstly obtained by dissolving pyrrolidine, NaOH, and $NaAlO_2$ in deionized water, then colloidal silica was added into the liquid and vigorously stirred at room temperature for 1 h. Finally, the obtained gel was transferred into the autoclave and subjected to crystallization in a tumbling oven (20 rpm) at 180 ^{o}C for 4 days. The solid products were collected by centrifugation, washed with deionized water until a near-neutral pH, and dried overnight at 60 °C. The sample was denoted as FER-F-0.

The zeolites were calcined in air at 550 °C for 5 h. To get the H-form of FER, calcined Na-form of the zeolite was exchanged with 1 M solution of NH_4Cl (1 g zeolite powder per 100 ml of the NH_4Cl solution, at 80 ^{o}C for 4 h). The procedure was repeated three times. After that, the samples were thoroughly washed with deionized water to remove the Na^+ and Cl^-. The solids were dried overnight at 60 °C and calcined in air at 550°C for 5 h.

Characterization.

The X-ray diffraction (XRD) patterns of zeolite samples were recorded on a PANalytical X'Pert Pro diffractometer using Cu-Kα radiation (k = 1.5418 Å, 45 kV, 40 mA). The tests were conducted at a scanning rate of 1 ^{o}/min in the region of 2θ = 5-40^{o}.

N_2 adsorption-desorption isotherms of zeolite samples were recorded on a Micromeritics ASAP 2020 automated gas adsorption analyzer. The samples were outgassed at 300 ^{o}C for 12 h prior to the test. The total surface area was calculated via the Brunauer Emmett Teller (BET) equation, the pore volume and the external surface area were calculated by the t-plot method.

Scanning electron microscopy (SEM) images of zeolite samples were obtained on a MIRA-LMH (TESCAN) scanning electron microscope (SEM).

Elemental analysis was tested by inductively coupled plasma–atomic emission spectroscopy (ICPAES), on an OPTIMA 4300 DV (Perkin–Elmer) instrument.

The TGA was performed on a SDT-Q600 instrument. Typically, a 5 mg sample was placed in an Al_2O_3 crucible. Then the tests were carried out in O_2/Ar (20 vol %/ 80 vol%) with a flow rate of 50 mL/min, and the temperature increased from room temperature to 800 ^{o}C with a heating rate of 20 ^{o}C /min.

Fourier Transform Infrared (FTIR) spectra of the zeolite samples were characterized by NicoletMagna 550-FT-IR spectrometer at a resolution of 4 cm^{-1}. The H-formed FER samples to be analyzed were pressed into self-supporting wafers (diameter: 2 cm, 20 mg). Then the samples were pre-treated at 100 ^{o}C (1 ^{o}C /min) for 2 h and 450 ^{o}C (1 ^{o}C / min) for 2 h, under secondary vacuum 10^{-6} torr. The adsorption of pyridine was performed at 150 °C and 300 °C, respectively. After establishing a pressure of 1 torr at equilibrium for pyridine, in order to remove the physisorbed species, the wafer was then evacuated at 150 °C. The adsorption of D_3-acetonitrile was performed at 25 °C. After establishing a pressure of 10 torr at equilibrium for D_3-acetonitrile, in order to remove the physisorbed species, the wafer was then evacuated at 25 °C. The amount of the probe molecules adsorbed on the Lewis and Brønsted acid sites was calculated by the corresponding integrated area of the bands in the IR spectra.

Transmission electron microscopy (TEM) and high-resolution transmission electron microscopy (HR-TEM) images of zeolite samples were recorded on a JEOL JEM-2100F electron microscope.

The ^{29}Si and ^{27}Al magic-angle-spinning (MAS) NMR spectra were recorded on a BRUKER AVANCE III 500 MHz, operating at 99.35 and 104.3MHz, respectively. Samples spun at 12 kHz using 4mm rotors. The experimental conditions were as follows: ^{29}Si (π/6 excitation pulses, 2048 transients, and 20 s recycle delay time), ^{27}Al (π/12 excitation pulses, 1000 transients, and 0.5 s recycle delay time). The ^{13}C MAS NMR and ^{1}H MAS NMR were performed on a Bruker Avance III 400WB, operating at 100.6 and 400.1 MHz, respectively. Sample spun at 10 kHz using 4mm rotors. The experimental conditions were as follows: ^{13}C (π/2 excitation pulses, 2048 transients, and 5 s recycle delay time), ^{1}H (π/2 excitation pulses, 1024 transients, and 5 s recycle delay time). Particularly, before the ^{1}H MAS NMR test, the samples were dehydrated at 380 ^{o}C under a dynamic vacuum with pressure below 10^{-5} torr for 10 h. Then the adsorption of D_3-acetonitrile was performed at 25 ^{o}C. After the D_3-acetonitrile loading, the samples were evacuated at 25 ^{o}C for 2 h to eliminate physisorbed D_3-acetonitrile.

The temperature-programmed desorption of ammonia (NH_3-TPD) was performed on a Micromeritics ChemiSorb 2720 chemisorption instrument. Typically, a 0.1 g sample was loaded into a quartz tube and was pre-treated at 550 ^{o}C for 1 h under continuous He flow (20 mL/min) to remove the adsorbed molecules. Then the sample was saturated with 5% NH_3/He at 150 °C. After that, the sample was purged with He at 150 °C for

1 h to eliminate the physically absorbed ammonia. Finally, the NH_3-TPD profile was recorded in flowing He (20 mL min^{-1}) from 150 to 700 °C at a heating rate of 10 °C min^{-1}.

Catalytic evaluation.

The skeletal isomerization of 1-butene to isobutene was performed in a fixed-bed reactor under atmospheric pressure. Typically, 0.1 g of the zeolite sample (sieve fraction, 0.45-0.90 mm) was placed in the center of the quartz reactor (5 mm i.d.). The H-form sample was pre-treated at 500 ^{o}C for 1 h, under continuous nitrogen flow. After that, the temperature was decreased to 400 ^{o}C. The mixture gas of 1-butene and nitrogen with a molar ratio of 1:1 was fed into the fixed bed. The weight hourly space velocity (WHSV) of 1-butene was set at 8 h^{-1}. The products were analyzed online by the gas chromatograph (7900 Techcomp) with a flame ionization detector (FID) and an Al_2O_3 capillary column.

The nature of organic compounds formed on the selected catalysts during the 1-butene isomerization reaction with the time-on-stream (TOS) of 120 min at 400 ^{o}C was *in situ* monitored by UV/vis and FTIR spectroscopy as described in refs 29 and 30.[29,30]

Results and discussion

Influence of fluoride content on the FER synthesis.

The FER samples synthesized with different NH_4F/SiO_2 molar ratios at 180 ^{o}C, are listed in Table S1 and their XRD patterns are presented in Fig. 2. Pure FER zeolite were obtained from the systems with NH_4F/SiO_2 ratio between 0 and 0.4. Upon increasing the NH_4F content (NH_4F/SiO_2=0.8), traces of MTN-type phase appeared in the product, and became the dominant phase at NH_4F/SiO_2=1.2. These results clearly show that there is a threshold of fluoride concentration, after which the purity of the samples is impacted. Moreover, compared with the FER zeolite synthesized without NH_4F (FER-F-0), the intensity of diffraction

peaks decreases, while the full width at half maximum (FWHM) of [200] reflection increases with increasing the NH_4F concentration in the synthesis system, indicating the decrease of the as-synthesized crystal dimension.

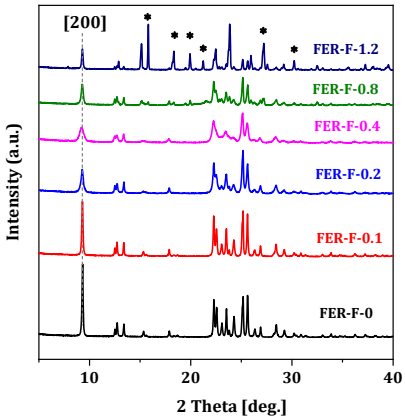

Fig. 2. XRD patterns of the FER zeolite samples synthesized with different NH_4F/SiO_2 molar ratios. *: MTN phase.

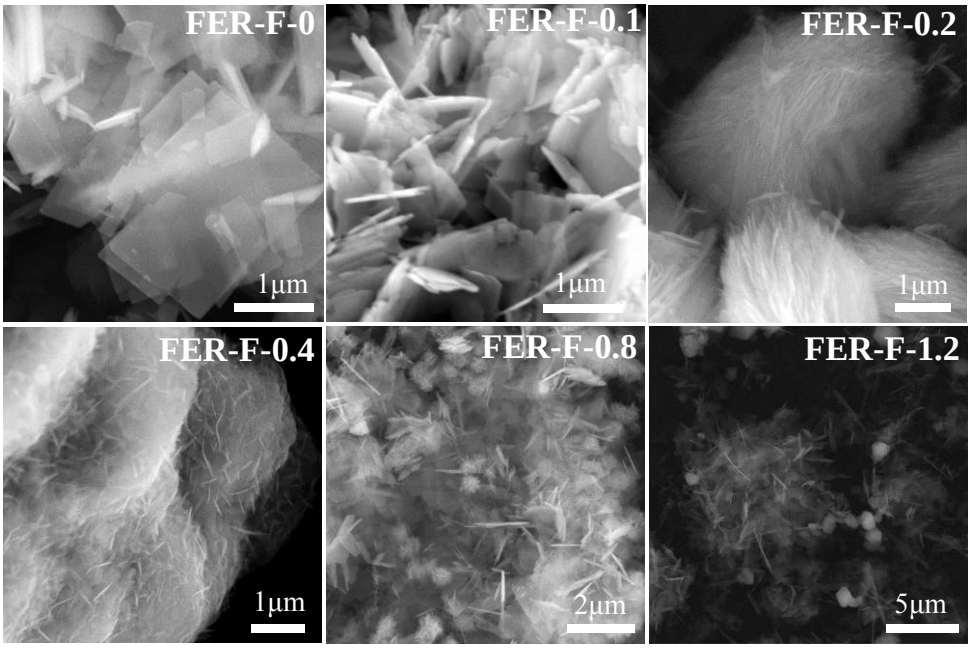

Fig. 3. SEM images of the FER zeolite samples synthesized with different NH_4F/SiO_2 molar ratios.

SEM was employed to study the morphology of FER zeolite crystals as a function of NH_4F concentration in the synthesis system (Fig. 3). FER-F-0 sample exhibits plate-like crystals with a size of around 2 μm. With increasing the NH_4F concentration, the crystal size gradually decreases. Noticeably, when the molar ratio of NH_4F/SiO_2 reaches 0.2, nanorod-like crystals are obtained with large agglomerates of about 5 μm. The SEM inspection is consistent with the XRD results and confirms the most significant decrease in the crystal size when the NH_4F/SiO_2 molar ratio reaches 0.2 and 0.4 (Fig. 3). Further increasing the molar ratio of NH_4F/SiO_2 to 0.8 and 1.2, results in an impurity phase that can be clearly distinguished. According to the XRD study, the impurity phase is MTN-type zeolite. Meanwhile, an obvious increase of the zeolite crystal sizes up to ~2 um and ~5 um, respectively, could also be observed with the further increase of the NH_4F concentration (Fig. 3). The SEM investigation confirms the results of the XRD study that there is an upper limitation of fluoride concentration for the synthesis of nanosized FER zeolite under the selected synthesis system. The threshold of NH_4F concentration is NH_4F/SiO_2=0.4 for the synthesis of well-crystallized and pure phase FER zeolite. The formation of the undesired MTN phase could be attributed to the pH value of the synthesis system, which decreases with the increase of NH_4F content, as shown in Fig. S1. When the synthesis is conducted in the fluoride-free system, the pH value of the synthetic gel is ~13.2. With increasing the dosage of NH_4F, the pH value of the synthetic gel gradually decreases from ~13.2 to ~11. When the molar ratio of NH_4F/SiO_2 is in the range of 0-0.4, the corresponding pH value are at ~13.2-12.1. Further increasing NH_4F/SiO_2 to 0.8 and 1.2 could decrease the pH value of the synthesis gel to 11.4 and 11, respectively. Combined with
the XRD and SEM results, it can be concluded that there may exist a suitable pH value region for the synthesis of nanosized FER zeolite at this synthesis system, which is above pH value of 12.

As discussed above, the FER-F-0.2 sample possesses both good crystallinity and small crystal size. This sample was selected to obtain detailed information on the nanorod-like crystals crystallographic orientation by TEM (Fig. 4). Fig. 4a and 4b reveal that the agglomerates observed in Fig. 3 are composed of uniform nanorod-like FER crystals. The well-defined lattice fringes, characteristic for a highly crystalline material, with an interplanar spacing of 0.94 ± 0.02 nm can be clearly observed in Fig. 4d. The Fast Fourier Transform (FFT) analysis of the selected area (red circle in Fig. 4d) shows that the as-synthesized FER zeolite crystals preferentially grew along the [0 1 $\bar{1}$] direction. The nanorod-like FER-F-0.2 crystals are elongated along the *c*-axis with the shortest length of ~70 nm. Thus, the length along the 10-MR ring channels was greatly reduced, compared with the samples FER-F-0 (~2000 nm) and FER-F-0.1 (~1000 nm). These results indicate that the addition of NH_4F into the synthesis system effectively shortens the length of the *c*-axis. Meanwhile, according to a previous study[31], the nanorod morphology offers more pore mouths per unit crystal surface, which is highly desirable in the catalytic application of FER zeolites. Hence, in comparison with the conventional plate-like crystals, the nanorod-like FER-F-0.2 sample exhibits much more 10-ring pore mouths at the boundary of FER zeolite crystals.

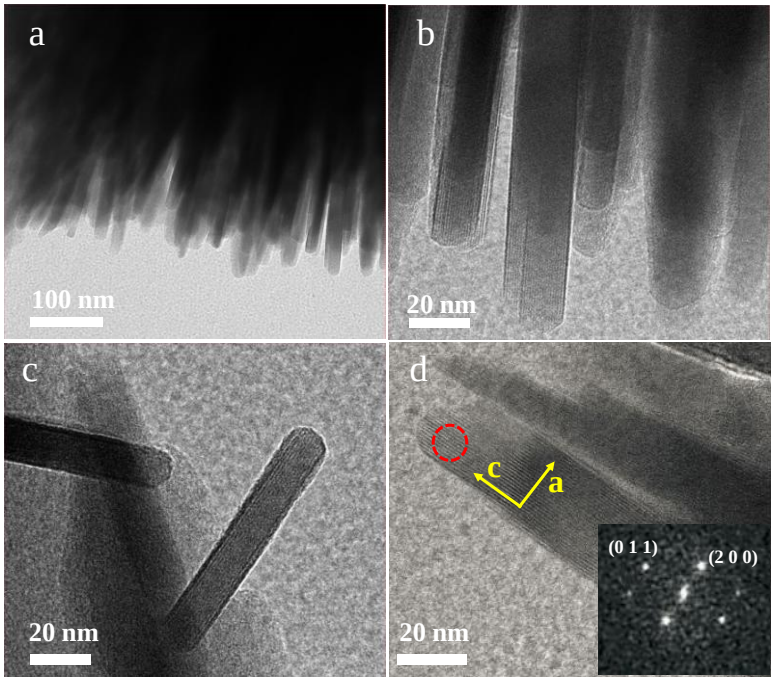

Fig. 4. The TEM (a, b, c) and HR-TEM (d) images of the FER-F-0.2 sample; the inset shows the FFT from the areas encircled in red corresponding to [0 1 $\bar{1}$] oriented FER crystals.

N_2 adsorption-desorption isotherms of calcined FER-F-0, FER-F-0.1, FER-F-0.2 samples are shown in Fig. S2. All three isotherms show a steep uptake at low relative pressure ($0 < p/p_0 < 0.01$), which is characteristic of the filling of micropores. The FER-F-0.2 sample exhibits an additional uptake at $0.5 < p/p_0 < 1$ pressure range with a hysteresis loop, which is most probably due to the mesopores between the heavily aggregated rod-like crystals. The porous characteristics and specific surface area of three FER zeolites are summarized in Table S2. All samples possess similar micropore volumes (0.13 m^2/g), which is characteristic of highly crystalline FER-type zeolite. The external surface area increases from 56 for the reference sample to 67 and 86 m^2/g for FER-F-0.1 and FER-F-0.2 samples, respectively. The rise of the external surface area with the increasing of fluoride concentration, is a consequence of the decrease of the zeolite crystal dimensions. Besides, compared to the sample FER-F-0, samples FER-F-0.1 and FER-F-0.2 show higher total pore volume due to the contribution of textural mesoporosity.

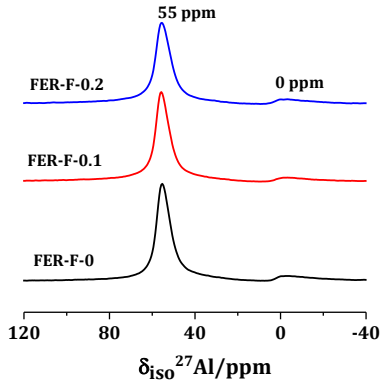

Fig. 5. ^{27}Al MAS NMR spectra of the calcined FER zeolites: FER-F-0, FER-F-0.1 and FER-F-0.2.

The Si/Al ratios of as-synthesized FER zeolite samples are also shown in Table S2. It can be found that the Si/Al ratios of samples obtained in fluoride-containing systems is slightly higher than that of the reference sample, which could be due to the lower conversion of aluminum source with the presence of fluoride.[32] The solid-state ^{27}Al and ^{29}Si MAS NMR spectroscopy was employed to highlight the local structure of framework aluminium and silicon atoms in the FER samples. As shown in Fig. 5, all three samples exhibit a dominant resonance at ~55 ppm in the ^{27}Al MAS NMR spectra, owing to the tetrahedrally coordinated framework aluminium. Simultaneously, only a weak signal due to the non-framework aluminium species occurred at ~0 ppm. This clearly indicates that most aluminium atoms can incorporate into the FER framework in both the fluorine-free and fluorine-containing systems.

As shown in Fig. 6, the ^{29}Si MAS NMR spectra display four peaks with chemical shifts at ~ -100, ~ -106, ~ -113 and ~ -116 ppm, which are assigned to Si(OH), Si(1Al), Si(0Al) and Si(0Al) species, respectively. The fitting of ^{29}Si MAS NMR spectra points out integrated intensities of ~1.5 % and ~2.0 % for the signal of Si(OH) in FER-F-0.2 and FER-F-0.1, respectively, which is much lower than that of the reference FER-F-0 sample (~4.3 %). According to the previous studies,[33–35] this is due to the specific effect of fluorine anion in zeolite framework, which reduces the number of defect species in the FER zeolite.

The ^{13}C MAS NMR spectroscopy was also employed to study the pyrrolidine state in the as-synthesized FER zeolites (Fig. S3). Two dominant signals at 25.0 and 48.8 ppm appear on all the

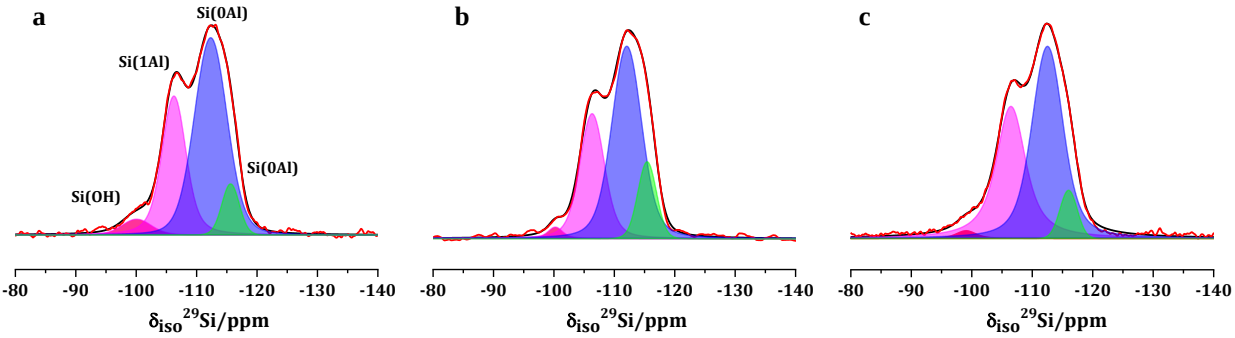

Fig. 6. ^{29}Si MAS NMR spectra of as-synthesized FER samples: (a) FER-F-0, (b) FER-F-0.1; (c) FER-F-0.2.

three samples. The former signal is assigned to the methylene (C_1) groups existed in pyrrolidine ring, while the latter is attributed to the methylene groups linked to the nitrogen atom in pyrrolidine ring.[36] These results confirm that the pyrrolidine molecule is well preserved within the zeolite pores. The TGA patterns of the samples are shown in Fig. S4. The weight loss at low-temperature (below 200 °C) for the samples FER-F-0, FER-F-0.1 and FER-F-0.2 are ~1.8%, ~1.2% and ~0.8%, respectively, which is assigned to the removal of the water molecules incorporated into the FER pores. Meanwhile, similar high-temperature weight losses of ~13.5% due to pyrrolidine combustion were recorded for all three samples.

Acidity analysis of the FER zeolites

D_3-acetonitrile (kinetic diameter 4.0 Å) [37] and pyridine (kinetic diameter 5.4 Å) [38] probe molecules are commonly used to estimate the acidity of zeolites. Compared to pyridine, the smaller D_3-acetonitrile can reach all acid sites of the FER zeolite, including those located in the 8-MR channels. Thus, D_3-acetonitrile can be used to detect the total acidity and the distribution of the Brønsted/Lewis sites in the FER zeolite. In contrast, as the molecule size is too bulky to penetrate the eight-membered ring, pyridine can only reach the acid sites located at the 10-MR channels and the external surface. Hence, the two probe molecules are chosen to study the acidity and quantify the number of acid sites of the two selected samples FER-F-0 and FER-F-0.2.

As shown in Fig. 7, both the IR spectra of adsorbed D_3-acetonitrile show five stretching models of ν(C≡N) in the range of 2200-2360cm^{-1}. The band at ~2323 cm^{-1} is attributed to the absorption of D_3-acetonitrile on the strong Lewis acid sites. The strong band at ~2297cm^{-1} is a typical characteristic of the strong interaction of D_3-acetonitrile with the Brønsted acid sites.[39] Besides, another three weaker bands located at ~2283, ~2265 and ~2248 cm^{-1} can be observed in the IR spectra, which reflect the interaction of D_3-acetonitrile with the defect sites of the FER zeolite, physisorbed D_3-acetonitrile, and C–D vibrations,[40] respectively. The numbers of Brønsted and Lewis acid sites were calculated from the area of the band centered at ~2297 cm^{-1} and ~2323 cm^{-1}, respectively, based on the molar absorption coefficient reported in the literature.[41] The total number of acid sites and the Brønsted and Lewis acid sites of the two zeolites are very similar (Table 1) and nearly identical with those found by the NH_3-TPD analysis (Fig. S5). The number of acid sites also correlates well with the Al content in the two zeolites.

Moreover, as established by previous studies,[42–44] the adsorption of D_3-acetonitrile on zeolite catalysts can be also used to discriminate the acid strength of Brønsted acid sites. In this case, the adsorption of the probe will result in the low-field shift of $\Delta\delta_{1H}$ of the ^{1}H MAS NMR signal of Si(OH)Al groups, namely a strong low-field shift of the $\Delta\delta_{1H}$ is corresponding to the high acid strength of the samples. Hence, the ^{1}H MAS NMR spectroscopy combined with D_3-acetonitrile adsorption was also employed to measure the acid strength of the FER zeolite samples. Fig. S6 shows the ^{1}H MAS NMR spectra of dehydrated samples recorded before and after loading with D_3-acetonitrile. After adsorption of the D_3-acetonitrile, the signal of the Si(OH)Al shifts from 4.1 ppm to 11.4 ppm, the identical low-field shift of the $\Delta\delta_{1H}$=7.3 ppm is observed for the two samples (FER-F-0 and FER-F-0.2), which indicates that the samples possess similar strength of Brønsted acid sites.

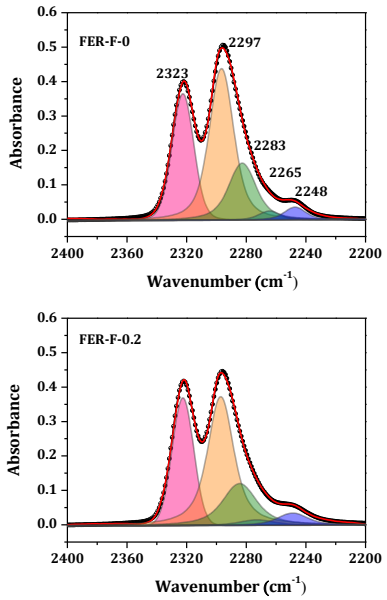

Fig. 7. FTIR spectra of D_3-acetonitrile adsorbed on the H-form of as-synthesized FER-F-0 and FER-F-0.2 samples.

Table 1. Acidity of H-FER zeolites determined by the FTIR after adsorption of different probe molecules.

sample	Brønsted acid sites (μmol/g)[a]		Lewis acid sites (μmol/g)[a]		Brønsted acid sites (μmol/g)[b]	Lewis acid sites (μmol/g)[b]	ACI[c]
	150 °C	300 °C	150 °C	300 °C			
FER-F-0	253	509	15	28	709	261	49.7
FER-F-0.2	301	458	42	82	664	238	65.7

[a] The acid amount is determined by using pyridine as the probe molecule

[b] The acid amount is determined by using D_3-acetonitrile as the probe molecule

[c] ACI is referred to the ratio of the concentration of Brønsted acid sites obtained at 150 °C to that obtained at 300 °C by the FTIR of pyridine adsorption

The acidity of the two selected samples was further investigated by the FTIR analysis of adsorbed pyridine. The pyridine provides information solely for the acid sites in 10-MR channel since it is too large to penetrate in the 8-MR channel of FER. The FTIR spectra of pyridine adsorbed on the H-form of FER-F-0 and FER-F-0.2 samples are shown in Fig. 8. The amount of pyridine adsorbed on Brønsted and Lewis acid sites was determined from the area of the 1545 cm^{-1} and 1454 cm^{-1} bands, respectively. At the adsorption temperature of 150 °C, the FER-F-0.2 sample exhibits a higher number of Brønsted acid sites than FER-F-0 sample (301 *vs* 253 μmol/g). This can be attributed to the smaller crystals and thus to the higher accessibility of the Brønsted acid sites in FER-F-0.2 sample. The pyridine accessibility was further tested at a higher temperature (300 °C). The detailed quantitative analysis of the results is summarized in Table 1. As shown, increasing the adsorption temperature leads to the pyridine molecules much easier diffusing into the 10-MR channels, and therefore, the amount of the Brønsted acid sites increases. The accessibility index (ACI) is an important characteristic to compare the accessibility of the

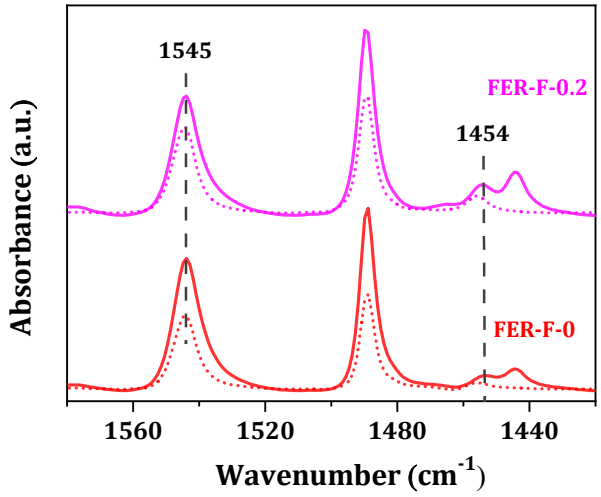

Fig. 8. FTIR spectra of pyridine adsorbed on the H-form of FER-F-0 and FER-F-0.2 samples (dotted line: 150 °C; solid line: 300 °C).

FER zeolites,[45–47] which is referred to the ratio of the concentration of Brønsted acid sites obtained at 150 °C to that obtained at 300 °C by the FTIR of pyridine adsorption. Obviously, the ACI of the FER-F-0.2 sample is much higher than that of the FER-F-0 sample (65.7 vs 49.7), indicating the better accessibility of the Brønsted acid sites of FER-F-0.2 than that of FER-F-0, which could be attributed to the much smaller size of nanorod-like FER-F-0.2 sample.

Catalytic performances in 1-butene skeletal isomerization

FER-F-0.2 sample exhibits better accessibility and larger external surface area than the reference FER-F-0 sample. Meanwhile, the nanorod-like morphology can also endow the FER zeolite with much more exposed 10-MR pore mouth. Ferrierite catalysts showed excellent catalytic performance in the skeletal isomerization of 1-butene to isobutene.[14,48] The reaction occurs in the 10-MR channels, namely at 10-MR pore mouths, because the carbonaceous deposits quickly block the microporous space once the reaction starts.[49,50] Therefore, 1-butene skeletal isomerization is an ideal probe reaction to evaluate the catalytic performance of the as-synthesized FER-F-0.2 with nanorod-like morphology. For comparison, FER zeolite synthesized by the conventional method, FER-F-0, was chosen as a reference sample.

Fig. 9 displays the 1-butene conversion, isobutene selectivity and yield as a function of TOS over FER-F-0 and FER-F-0.2. FER-F-0 sample exhibits a higher initial conversion of 1-butene than FER-F-0.2 sample (68% *vs* 62%). As the Brønsted acid located in the 10-MR of FER zeolite plays an important role in the skeletal isomerization of 1-butene, the higher initial 1-butene conversion on FER-F-0 should be attributed to the higher density of Brønsted acid in the 10-MR channel, 509 μmol/g for FER-F-0 in respect to 458 μmol/g for FER-F-0.2. However, with the progress of the 1-butene conversion, FER-F-0.2 sample exhibits much better resistance to deactivation and higher selectivity than FER-F-0 sample. This could be due to the better accessibility of Brønsted acid sites in the 10-MR channels, larger external surface area as well as larger number of the 10-MR pore mouth in the FER-F-0.2 sample. Consequently, a steadily high yield of isobutene with better catalytic stability could be achieved over FER-F-0.2 zeolite catalyst.

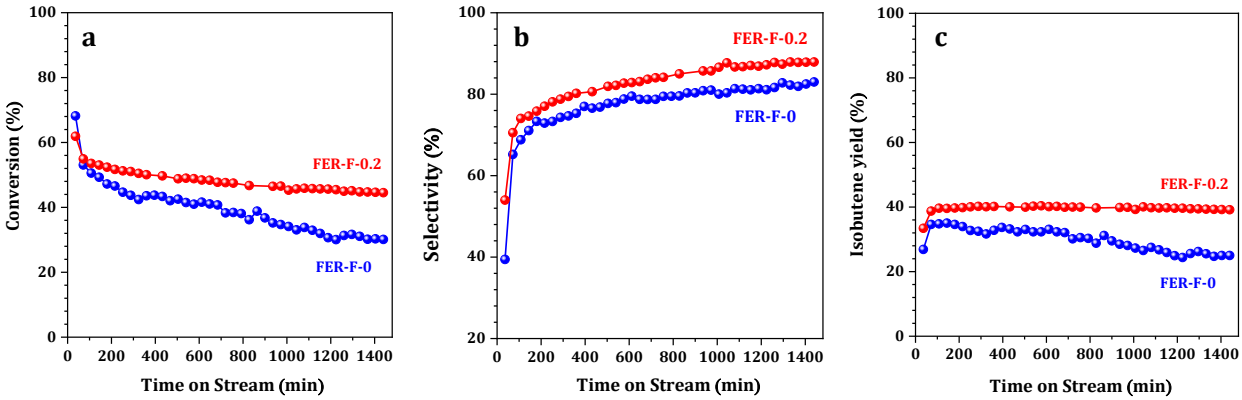

Fig. 9. Catalytic performances of 1-butene skeletal isomerization over as-synthesized FER-F-0 and FER-F-0.2 samples: (a) 1-butene conversion; (b) isobutene selectivity; (c) isobutene yield.

The capability of coke tolerance was further investigated by TGA analysis of the spent catalysts. As shown in Fig. S7, the weight loss below 200 °C is due to the desorption of volatile compounds, while the weight loss at higher temperatures of 400-800 °C is attributed to occluded coke compounds. Compared to the FER-F-0 sample, the nanorod-like FER-F-0.2 sample exhibits much less coke deposition (7.9 % vs 10.0 %). To compare the coke formation during the reaction more directly, the average coke accumulation rate (R_{coke}) of the two samples was evaluated. As shown in the Table S3, it is obvious that the nanorod-like FER-F-0.2 sample shows a lower R_{coke} than conventional sample FER-F-0 (0.357 *vs* 0.463 mg/h). Therefore, one may conclude that the nanorod-like FER-F-0.2 catalyst exhibits better coke tolerance in the 1-butene skeletal isomerization than FER-F-0 catalyst. This could be explained as that the special nanorod-like morphology could provide a much short diffusion path along the 10-MR channel and improve the accessibility to the active sites in 10-MR channel. The results are also in good agreement with the higher catalyst stability of the the FER-F-0.2 sample (Figure 9).

The nature of the occluded organic intermediates formed during the process of 1-butene isomerization over FER-F-0 and FER-F-0.2 samples was investigated by *in situ* UV/Vis and FTIR spectroscopy. The *in situ* UV/Vis spectra recorded at 400 °C over the two samples with a TOS of 120 min are shown in Fig. 10. Similar organic intermediates were formed during the 1-butene isomerization over the two samples, as indicated by UV/Vis bands at ~280, 380-420, 450-500 and 570-650 nm. According to the previous studies,[51–53] the band at ~280 nm was assigned to monoenylic carbenium ions or polyalkylaromatics species, while the bands at 380-420 nm were attributed to benzene-based carbenium ions and polycyclic aromatics. Bands at 450-500 and 570-650 nm hint at the formation of polycyclic aromatics, and the former is assigned to naphthalenic carbenium ions, while the latter could be attributed to phenanthrenic and pyrenic carbenium ions. The concentrations of all the aforementioned organic species, reflected by the intensities of the corresponding UV/Vis bands, vary obviously with the progress of 1-butene conversion. Monoenylic carbenium ions/polyalkylaromatics species (~280 nm) are rapidly formed even in the initial period of the 1-butene conversion. With the progress of 1-butene conversion, the bands of monoenylic carbenium ions/polyalkylaromatics increase, then gradually decrease. Simultaneously, benzene-based carbenium ions (380-420 nm) and polycyclic aromatic-based carbenium ions (450-500 and 570-650 nm) are gradually formed, and a rapid accumulation of polycyclic aromatics (450-650 nm) occur.

These observations clearly demonstrate that the polyalkylaromatics and the corresponding benzene-based carbenium ions formed during the initial period of 1-butene conversion are gradually transferred to phenanthrenic and pyrenic carbenium ions with the further progress of the reaction. As is well known, polycyclic aromatics can gradually cover the acid sites or block the zeolite cages/channels, thus causing the catalyst deactivation eventually. In comparison with FER-F-0 sample, a slow accumulation of polycyclic aromatics occurs over FER-F-0.2, which agrees well with the catalytic activity (Figure 9) and TGA results (Table S3 and Figure S7), where a better catalyst stability and a slow deactivation ratio occurs.

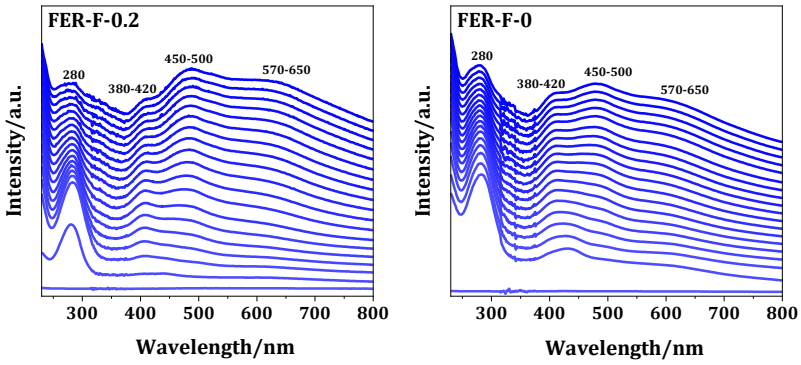

Fig. 10. In situ UV/vis spectra recorded during the 1-butene skeletal isomerization on FER zeolite samples up to TOS = 120 min at the reaction temperature of 400 °C.

The *in situ* FTIR spectra of the organic species adsorbed and occluded on the two FER samples at 400 °C with a TOS of 120 min are shown in Fig. 11. The bands at approximately 1500 cm^{-1} attributed to C=C vibrations of aromatics rapidly occur over the two samples.[54] These results clearly indicate that 1-butene oligomerization and subsequent cyclization occur immediately upon starting the 1-butene flowing. With the progress of 1-butene conversion, new bands at ~1550 and ~1580 cm^{-1} assigned to the C=C vibrations of the polycyclic aromatics start to appear.[55,56] These bands reveal a rapid accumulation of polycyclic aromatics during the 1-butene isomerization reaction over FER samples. In comparison with FER-F-0.2, two additional bands at ~1650 and ~1460 cm^{-1} also occur over FER-F-0 sample. The former can be attributed to π-coordinated butene or the olefinic oligomers[54], while the latter is assigned to C-H bending vibrations of the CH_2 or CH_3 groups, indicating much more large aromatics with more branches are formed over FER-F-0 sample, which can rapidly make the acid sites inaccessible to 1-butene molecules, and thus causing the catalyst deactivation finally, in good agreement with the TGA and *in situ* UV/Vis results (vide supra).

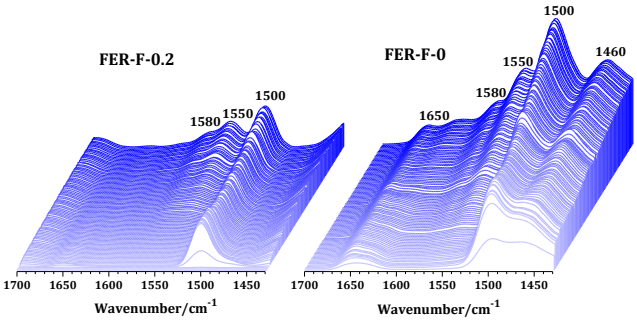

Fig. 11. In situ FTIR spectra recorded during the 1-butene skeletal isomerization on FER zeolite samples up to TOS = 120 min at the reaction temperature of 400 °C.

Conclusions

A fluoride-assisted synthesis strategy to nanosized FER-type zeolite crystal is successfully developed. The effects of fluoride concentration on the morphology and physicochemical properties of FER zeolite are investigated. The best result in terms of small crystals and high crystallinity is obtained at NH_4F/SiO_2 ratio of 0.2. Under this condition, the resultant sample shows a nanorod-like morphology, and the dimension along the c-axis is reduced to ~70 nm. A much higher NH_4F concentration (at NH_4F/SiO_2>0.4) leads to an undesired phase in the final products.

The nanorod-like FER zeolite possesses much higher external area, larger number of the 10-MR pore mouth per unit crystal surface and better accessibility to the acid sites, in comparison to the conventional FER zeolite obtained with the same SDA. The nanorod-like FER zeolite was found to be much more efficient for the skeletal isomerization of 1-butene to isobutene than the conventional crystals, which is related to the particular morphology achieved by the NH_4F-assisted synthesis. Besides, lower amount of organic deposits on the spent nanorod-like catalyst were revealed by the TGA analysis than the conventional FER zeolite catalyst (7.9% *vs* 10.0%). Meanwhile, the R_{coke} analysis indicates that the nanorod-like catalyst has a much lower R_{coke} than the conventional FER catalyst (0.357 *vs* 0.463 mg/h). Thus, the set of catalytic results unambiguously prove the superior catalytic potential of nanosized nanorod-like FER in respect to conventional micronsized plate-like crystals.

Conflicts of interest

There are no conflicts to declare.

Acknowledgments

We acknowledge the National Natural Science Funds of China (22172079, 21872072, 22025203), and the China Scholarship Council for supporting the work. V.V. acknowledges the financial support from the Industrial Chair ANR-TOTAL “NanoClean Energy” (ANR-15-CE06-0004).

References

1 D. W. Breck, *Zeolite Molecular Sieves: Structure, Chemistry, and Use*; Wiley: New York, 1974
2 A. Corma, *Chem. Rev.*, 1997, **97**, 2373–2419.
3 V. Van Speybroeck, K. Hemelsoet, L. Joos, M. Waroquier, R. G. Bell and C. R. A. Catlow, *Chem. Soc. Rev.*, 2015, **44**, 7044–7111.
4 V. Valtchev and L. Tosheva, *Chem. Rev.*, 2013, **113**, 6734–6760.
5 J. Přech, P. Pizarro, D. P. Serrano and J. Áejka, *Chem. Soc. Rev.*, 2018, **47**, 8263–8306.
6 J. Pérez-Ramírez, C. H. Christensen, K. Egeblad, C. H. Christensen and J. C. Groen, *Chem. Soc. Rev.*, 2008, **37**, 2530–2542.
7 C. Jo, J. Jung, H. S. Shin, J. Kim and R. Ryoo, *Angew. Chem., Int. Ed.,* 2013, **52**, 10014–10017.
8 H. Awala, J. P. Gilson, R. Retoux, P. Boullay, J. M. Goupil, V. Valtchev and S. Mintova, *Nat. Mater.*, 2015, **14**, 447–451.
9 R. Li, N. Linares, J. G. Sutjianto, A. Chawla, J. Garcia-Martinez and J. D. Rimer, *Angew.Chem., Int. Ed.,* 2018, **57**, 11283–11288.
10 M. Debost, P. B. Klar, N. Barrier, E. B. Clatworthy, J. Grand, F. Laine, P. Brázda, L. Palatinus, N. Nesterenko, P. Boullay and S. Mintova, *Angew. Chem., Int. Ed.,* 2020, **59**, 23491–23495.
11 Q. Zhang, A. Mayoral, O. Terasaki, Q. Zhang, B. Ma, C. Zhao, G. Yang and J. Yu, *J. Am. Chem. Soc.*, 2019,**141**, 3772–3776.
12 H. Xu, J. Zhu, L. Zhu, E. Zhou and C. Shen, *Molecules*, 2020, **25**, 19–25.
13 M. Guisnet, P. Andy, N. S. Gnep, E. Benazzi and C. Travers, *J. Catal.*, 1996, **158**, 551–560.
14 H. H. Mooiweer, K. P. de Jong, B. Kraushaar-Czarnetzki, W. H. J. Stork and B. C. H. Krutzen, *Stud. Surf. Sci. Catal.*, 1994, **84**, 2327–2334.
15 L. Domokos, L. Lefferts, K. Seshan and J. A. Lercher, *J. Catal.*, 2001, **197**, 68–80.
16 J. Kim, H. Ham, H. S. Jung, Y. Wang, Y. He, N. Tsubaki, S. J. Cho, G. Y. Han and J. W. Bae, *Catal. Sci. Technol.*, 2018, **8**, 3060–3072.
17 H. Ham, H. S. Jung, H. S. Kim, J. Kim, S. J. Cho, W. B. Lee, M. J. Park and J. W. Bae, *ACS Catal.*, 2020, **10**, 5135–5146.

18 R. Bastiani, Y. L. Lam, C. A. Henriques and V. T. Da Silva, *Fuel*, 2013, **107**, 680–687.
19 Y. Lee, M. B. Park, P. S. Kim, C. Fernandez, I. Nam and S. B. Hong, , ACS Catal. 2013, 3, 617−621.
20 V. J. Margarit, M. R. Díaz-Rey, M. T. Navarro, C. Martínez and A. Corma, *Angew.Chem., Int.Ed.* 2018, **57**, 3459–3463.
21 H. Xu, W. Chen, G. Zhang, P. Wei, Q. Wu, L. Zhu, X. Meng, X. Li, J. Fei, S. Han, Q. Zhu, A. Zheng, Y. Ma and F. S. Xiao, *J. Mater. Chem. A*, 2019, **7**, 16671–16676.
22 E. Catizzone, S. Van Daele, M. Bianco, A. Di Michele, A. Aloise, M. Migliori, V. Valtchev and G. Giordano, *Appl. Catal. B Environ.*, 2019, **243**, 273–282.
23 Y. Wang, Y. Gao, W. Chu, D. Zhao, F. Chen, X. Zhu, X. Li, S. Liu, S. Xie and L. Xu, *J. Mater. Chem. A*, 2019, **7**, 7573–7580.
24 E. Catizzone, M. Migliori, T. Mineva, S. van Daele, V. Valtchev and G. Giordano, *Microporous Mesoporous Mater.*, 2020, **296**, 109988.
25 T. C. Pham, H. S. Kim and K. B. Yoon, *Science*, 2011, **334**, 1533-1539.
26 M. Zhou, D. Korelskiy, P. Ye, M. Grahn and J. Hedlund, *Angew. Chem., Int. Ed*. 2014, **53**, 3492 –3495.
27 Y. Chen, G. Zhu, Y. Peng, X. Yao and S. Qiu, *Microporous Mesoporous Mater.*, 2009, **124**, 8–14.
28 W. Dai, C. Kouvatas, W. Tai, G. Wu, N. Guan, L. Li and V. Valtchev, *J. Am. Chem. Soc.*, 2021, **143**, 1993–2004.
29 L. Yang, T. Yan, C. Wang, W. Dai, G. Wu, M. Hunger, W. Fan, Z. Xie, N. Guan and L. Li, *ACS Catal.*, 2019, **9**, 6491–6501.
30 T. Yan, L. Yang, W. Dai, G. Wu, N. Guan, M. Hunger and L. Li, *ACS Catal.*, 2019, **9**, 9726–9738.
31 Y. Lee, M. B. Park, P. S. Kim, A. Vicente, C. Fernandez, I. S. Nam and S. B. Hong, *ACS Catal.*, 2013, **3**, 617–621.
32 J.L. Guth, H. Kessler, J.M. Higel, J.M. Lamblin, J. Patarin, A. Seive, J.M. Chezeau, R. Wey, *Zeolite Synthesis***,** American Chemical Society, Washington, DC, 1989.
33 J. M. Chézeau, L. Delmotte, J. L. Guth and M. Soulard, *Zeolites*, 1989, **9**, 78–80.
34 M. A. Camblor and L. A. Villaescusa, *Top. Catal.*, 1999, **9**, 59–76.
35 P. Caullet, J. L. Paillaud, A. Simon-Masseron, M. Soulard and J. Patarin, *C. R. Chim.,* 2005, **8**, 245–266.
36 D. Rima, D. Djamal, D. Fatiha, Mater. Res. Express. 2018, **6**, 035017.
37 M. Shamzhy, J. Přech, J. Zhang, V. Ruaux, H. El-Siblani and S. Mintova, *Catal. Today*, 2020, **345**, 80–87.
38 I. Miletto, G. Paul, S. Chapman, G. Gatti, L. Marchese, R. Raja and E. Gianotti, *Chem. - Eur. J.,* 2017*,* **23***,* 9952–9961.
39 A. G. Pelmenschikov, R. A. Van Santen, J. Jänchen and E. Meijer, *J. Phys. Chem.*, 1993, **97**, 11071–11074.
40 J. Chen, J. M. Thomas and G. Sankar, *J. Chem. Soc. Faraday Trans.*, 1994, **90**, 3455–3459.
41 B. Wichterlová, Z. Tvarůžková, Z. Sobalík and P. Sarv, *Microporous Mesoporous Mater.*, 1998, **24**, 223–233.
42 C. Pazè, A. Zecchina, S. Spera, A. Cosma, E. Merlo, G. Spanò and G. Girotti, *Phys. Chem. Chem. Phys.*, 1999, **1**, 2627–2629.
43 W. Dai, X. Sun, B. Tang, G. Wu, L. Li, N. Guan and M. Hunger, *J. Catal.*, 2014, **314**, 10–20.
44 Y. Jiang, J. Huang, W. Dai and M. Hunger, *Solid State Nucl. Magn. Reson.*, 2011, **39**, 116–141.
45 Y. P. Khitev, I. I. Ivanova, Y. G. Kolyagin and O. A. Ponomareva, *Appl. Catal., A,* 2012, **441**–**442**, 124–135.
46 Y. P. Khitev, Y. G. Kolyagin, I. I. Ivanova, O. A. Ponomareva, F. Thibault-Starzyk, J. P. Gilson, C. Fernandez and F. Fajula, *Microporous Mesoporous Mater.*, 2011, **146**, 201–207.
47 I. I. Ivanova and E. E. Knyazeva, *Chem. Soc. Rev.*, 2013, **42**, 3671–3688.
48 C. L. O'Young, R. J. Pellet, D. G. Casey, J. R. Ugolini and R. A. Sawicki, *J. Catal.*, 1995, 151, 467–469.
49 L. Domokos, L. Lefferts, K. Seshan and J. A. Lercher, *J. Mol. Catal. A Chem.*, 2000, **162**, 147–157.
50 R. J. Pellet, D.G. Casey, H. Huang R.V. Kessler, E.J. Kuhlman C.L. Oyoung, R.A.Sawicki and J.R.Ugolini, *J. Catal.*, 1995, **157**, 423–435.
51 D. Mores, J. Kornatowski, U. Olsbye and B. M. Weckhuysen, *Chem. - Eur. J.,* 2011, **17**, 2874–2884.
52 V. Van Speybroeck, K. Hemelsoet, K. De Wispelaere, Q. Qian, J. Van der Mynsbrugge, B. DeSterck, B. M. Weckhuysen and M. Waroquier, *ChemCatChem*, 2013, **5**, 173–184.
53 E. Borodina, H. Sharbini Harun Kamaluddin, F. Meirer, M. Mokhtar, A. M. Asiri, S. A. Al-Thabaiti, S. N. Basahel, J. Ruiz-Martinez and B. M. Weckhuysen, *ACS Catal.*, 2017, **7**, 5268–5281.
54 F. C. Meunier, L. Domokos, K. Seshan and J. A. Lercher, *J. Catal.*, 2002, **211**, 366–378.
55 P. Ivanov and H. Papp, *Appl. Surf. Sci.*, 2001, **179**, 234–239.
56 C. Pazè, B. Sazak, A. Zecchina and J. Dwyer, *J. Phys. Chem. B*, 1999, **103**, 9978–9986.